Natural convection in heterogeneous porous stratum

Tianpei Cheng [1], Haijian Yang [2,*] Mei Zhang, [3] and Ke Xu [4,†]
[1] School of Mathematical Sciences, Peking University, Beijing 100871, People's Republic of China
[2] School of Mathematics, Hunan University, Changsha, Hunan 410082, People's Republic of China
[3] School of Mathematics and Statistics, Henan Normal University, Xinxiang, Henan 453007, People's Republic of China
[4] School of Mechanics and Engineering Science, Peking University, Beijing 100871, People's Republic of China

(Received 1 February 2026; accepted 26 May 2026; published 22 June 2026)

Buoyancy-driven natural convection in porous media, known as Rayleigh-Darcy convection (RDC), is ubiquitous in geological and engineering systems, where it is induced by natural or anthropogenic temperature and concentration gradients under which higher density fluid lays above lower density fluid. Although medium heterogeneity is widely recognized as a key factor governing subsurface fluid flow, its role in regulating RDC remains poorly understood. Using high-resolution numerical simulations over a broad range of Rayleigh numbers (Ra), we show that the interplay between the permeability correlation length ($\mathcal{L}$) and the characteristic flow-structure length fundamentally controls RDC dynamics. In the stable convective-cell regime ($Ra < 1300$), $\mathcal{L}$ constrains the horizontal extent of convection cells and therefore modifies transport efficiency. In the transition regime ($1300 \leqslant Ra \leqslant 7500$), heterogeneity disrupts the transverse coherence of the boundary layers and suppresses the merging of microplumes into large-scale megaplumes, which significantly amplifies convective instability and enhances transport. In the chaotic regime ($Ra > 7500$), heterogeneity with small $\mathcal{L}$ has a negligible effect, whereas that with large $\mathcal{L}$ regulates the boundary-layer thickness through local permeability variations. These results provide a unified physical framework for understanding how heterogeneity regulates buoyancy-driven convection in porous media.

DOI: 10.1103/vp58-v6xc

I. INTRODUCTION

Rayleigh-Darcy convection (RDC) refers to buoyancy-driven flow in fluid-saturated porous media, arising when a higher-density fluid overlies a lower-density fluid, typically due to geothermal temperature gradients or imposed concentration gradients. As one of the fundamental transport mechanisms in porous systems, it plays a central role in a wide range of geophysical and engineering processes [1,2]. Representative applications include geological carbon sequestration [3–5], where dissolved CO_2 drives convective mixing in saline aquifers, groundwater contamination and remediation [6,7], geothermal energy extraction [8,9], and thermal management in porous composites [10,11].

Many numerical, experimental, and theoretical approaches have been reported for RDC in homogeneous media. Classic theories measure the driving buoyancy forcing with the Rayleigh number, Ra [12–14], which characterizes the relative strength of buoyancy-driven flow to molecular

*Contact author: haijianyang@hnu.edu.cn
†Contact author: kexu1989@pku.edu.cn

diffusion. Once the Ra exceeds a critical value ($\approx 4\pi^2$), natural Rayleigh-Darcy convection is triggered [15,16] and evolves into statistically steady flow structures [17,18]. These structures, and the transport regimes they give rise to, form the foundation of theoretical descriptions of RDC.

A key consequence of these flow structures is a substantial enhancement of scalar transport. Numerical simulations show that the enhanced transport, expressed through the Nusselt number (Nu), exhibits distinct power-law behaviors over different ranges of Rayleigh numbers. For moderately large Ra ($500 \lesssim Ra \lesssim 1200$), Nu grows sublinearly with Ra, whereas for $1255 \leqslant Ra \leqslant 4 \times 10^4$ [17,19], the transport asymptotically returns to a linear scaling. Prior studies further demonstrate that boundary conditions, reactive behaviors, and lateral dispersion strongly influence the resulting flow patterns [20–24].

Despite these insights, most numerical investigations have been conducted under idealized, laterally uniform conditions, and the widely reported scaling relations are almost exclusively derived from homogeneous media. However, natural and engineered porous media are inherently heterogeneous, with permeability varying spatially over orders of magnitude. As permeability directly regulates local flow, it may induce significant deviations in RDC patterns from those in homogeneous media. Although the influence of heterogeneity on RDC and scalar transport efficiency remains not fully understood, several recent studies [25–27] have highlighted the important role of heterogeneity in Rayleigh-Bénard instability and reactive convective dissolution. Extending this line of research, the present work further examines how permeability heterogeneity governs RDC dynamics and the associated transport efficiency. Here we present a parallel numerical approach to investigate the effects of permeability heterogeneity on scalar dissipation in Rayleigh-Darcy convection. Specially designed numerical experiments are used to examine changes in dissipation scaling relative to the homogeneous case.

II. METHODOLOGY

We investigate the influence of permeability heterogeneity on flow patterns and scalar transport in two-dimensional Rayleigh-Darcy convection within a fluid-saturated porous medium of uniform porosity ϕ and heterogeneous permeability κ. The domain has height H and width L with aspect ratio $L/H = 5$.

A. Governing equations

We nondimensionalize the system. The layer height H is adopted as the characteristic length scale. We denote the dynamic viscosity of the fluid by μ, the gravitational acceleration by g, and the molecular diffusivity of the passive scalar by D. Minimum and maximum dimensional scalar concentrations are denoted by $c^*_{\min}$ and $c^*_{\max}$, respectively, which results in density contrast $\Delta\rho_c = \rho^*(c^*_{\max}) - \rho^*(c^*_{\min})$ that drives the RDC. We thus introduce the characteristic velocity $U^* = g\,\Delta\rho_c/\mu$, and nondimensionalize the velocity as $\mathbf{u} = \mathbf{u}^*/U^*$. The corresponding characteristic time scale is defined as $t_c = t^*/(\phi H/U^*)$. The concentration is normalized as $c = (c^* - c^*_{\min})/\Delta c$, where $\Delta c = c^*_{\max} - c^*_{\min}$. Under this nondimensionalization, the dynamics are governed by the Rayleigh number defined as $Ra = (g\Delta\rho_c H)/(\phi D\mu)$, which characterizes the strength of buoyancy-driven convection relative to molecular diffusion. The dimensionless governing equations are

$$\frac{\partial c}{\partial t} + \nabla \cdot \left(c\mathbf{u} - \frac{1}{Ra}\nabla c\right) = 0, \quad \nabla \cdot \mathbf{u} = 0, \quad \mathbf{u} = -\kappa_{\mathrm{act}}(\nabla p + c\,\mathbf{i}), \tag{1}$$

where $\mathbf{i}$ is the vertical unit vector. The concentration is fixed at the top ($c = 1$) and bottom ($c = 0$) boundaries, while no-flux conditions are imposed on the pressure field. Initially, the concentration increases linearly from the bottom boundary to the top boundary, with a small random perturbation added to break symmetry and promote the onset of convection. This configuration produces an unstable vertical density stratification. Periodic boundary conditions are applied in the horizontal direction. To enable a consistent comparison of Rayleigh-Darcy convection (RDC) in homogeneous and heterogeneous porous media, we normalize the local permeability as $\kappa_{\mathrm{act}} = \kappa/\kappa_{\mathrm{eff}}$, where κ_{eff}

is the effective permeability in the vertical direction. The effective permeability is obtained by solving a steady Darcy flow driven by a prescribed pressure drop between the top and bottom boundaries, with no-flux conditions imposed on the lateral boundaries. It is then defined by matching the resulting domain-averaged vertical flux to that of an equivalent homogeneous medium. For homogeneous media, the effective permeability is fixed to $\kappa_{\text{eff}} = 1$.

B. Heterogeneity

In the main text, we primarily consider permeability ranges of $\kappa \in [0.1, 10]$, $[0.5, 2]$, and $[0.9, 1.1]$. The permeability κ is generated from two points, $\mathbf{x} = (x^*, y^*)$ and $\mathbf{x}_1 = (x_1^*, y_1^*)$; the normalized separation is defined as

$$h = \frac{\sqrt{(x_1^* - x^*)^2 + (y_1^* - y^*)^2}}{\mathcal{L}};$$

and the corresponding covariance is given by

$$C_Z(\mathbf{x}_1, \mathbf{x}) = \exp(-h^2).$$

A realization of the Gaussian field Z is generated sequentially via

$$Z(u_i) = \sum_{j<i} \lambda_j(u_i) Z(u_j) + \sigma_E(u_i) U(u_i), \tag{2}$$

where $\lambda_j(u_i)$ are the Kriging weights computed from C_Z, $\sigma_E(u_i)$ is the Kriging variance, and $U(u_i) \sim \mathcal{N}(0, 1)$ are independent Gaussian samples with $\mathcal{N}(0, 1)$ being the standard normal distribution. The heterogeneous permeability field is then obtained by linearly rescaling Z to the desired range,

$$\kappa(\mathbf{x}) = \kappa_{\min} + (Z(\mathbf{x}) - Z_{\min}) \frac{\kappa_{\max} - \kappa_{\min}}{Z_{\max} - Z_{\min}}, \tag{3}$$

which ensures that κ stays within $[\kappa_{\min}, \kappa_{\max}]$ while preserving the spatial correlation structure. Heterogeneity is thus characterized by two parameters: the correlation length $\mathcal{L}$, controlling spatial connectivity, and the range of permeability $[\kappa_{\min}, \kappa_{\max}]$, controlling its variability. For each value of $\mathcal{L}$, the corresponding permeability field is generated using a sequential Gaussian simulation (SGS) procedure [28,29], which enables systematic control of the spatial correlation structure of the medium, different correlation lengths $\mathcal{L}$ generate distinct permeability fields κ and corresponding concentration fields, as shown in Fig. 1.

C. Numerical implementation and validation

The governing partial differential equations (PDEs) are spatially discretized using a cell-centered finite difference scheme and temporally discretized with a fully implicit Euler scheme [30,31], and then numerically solved by our in-house code. The resulting nonlinear systems are solved by the Newton-Krylov algorithm and an overlapping restricted additive Schwarz preconditioner with subspace correction [32]. The parallel implementation is built on the open-source Portable, Extensible Toolkit for Scientific Computation (PETSc) library [33]. In the simulations, the Rayleigh number varies over the range $60 \leqslant Ra \leqslant 1 \times 10^4$ for the homogeneous case. After the flow reaches a statistically steady state, data from the homogeneous simulations are used to evaluate the Nusselt number Nu, defined as the horizontally averaged dimensionless vertical concentration gradient at the top and bottom boundaries [17], and the Péclet number Pe, defined as the root-mean-square characteristic velocity within the domain [21]. Their dependence on the Rayleigh number in a homogeneous medium, shown in Figs. 2(a) and 2(b), is in excellent agreement with previous studies [4,13,18,34], thereby validating the numerical implementation.

Figure 2(c) shows the permeability field for the case with correlation length $\mathcal{L} = 0.0348$ and permeability range $\kappa \in [0.1, 10]$, in which pronounced spatial heterogeneity is evident. The

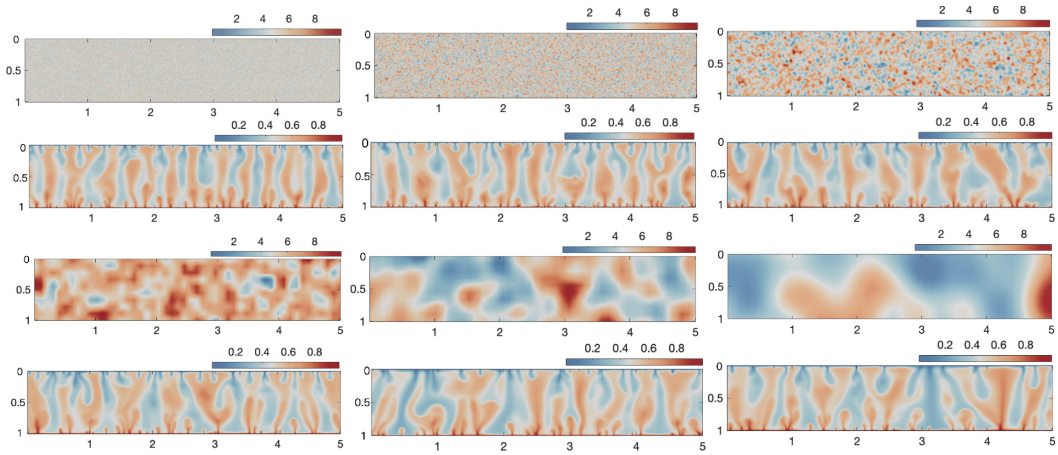

FIG. 1. The first and third rows show the permeability fields for $\mathcal{L} = 0.0029,\ 0.0161,\ 0.0348$ and $\mathcal{L} = 0.161,\ 0.232,\ 0.464$, respectively. The corresponding concentration fields are shown directly below each permeability field in the second and fourth rows. All concentration fields are taken at $t^*/t_c = 100$ and $Ra = 5000$.

corresponding time-averaged concentration and dimensionless velocity fields at $t^*/t_c = 100$ for $Ra = 5000$ are shown in Figs. 2(d) and 2(e), respectively. The corresponding temporal evolution of the scalar dissipation rate χ is shown in Fig. 2(f). Here, χ is defined as the domain- and time-averaged value of $|\nabla c|^2$ over a statistically steady interval [13]. The temporal evolution of the fluctuation energy E is plotted in Fig. 2(g), where the quantity E is defined as the instantaneous spatially integrated variance of the concentration field relative to its steady-state mean. Once the convection enters this steady regime, χ remains nearly constant for the remainder of the simulation.

III. RESULTS AND DISCUSSION

A comprehensive set of simulations is performed for Rayleigh numbers in the range $60 \leqslant Ra \leqslant 2 \times 10^4$, considering both homogeneous and heterogeneous permeability fields. Figure 3(a) presents the time-averaged rescaled scalar dissipation χ/χ_{uni} for different Rayleigh numbers after the flow reaches a statistically steady state, where χ_{uni} denotes the scalar dissipation obtained in the homogeneous medium. Unless otherwise stated, all analyses in this section are based on statistically steady states. For small correlation lengths ($\mathcal{L} < 0.1$), the scalar dissipation χ is nearly identical to χ_{uni} at low Rayleigh numbers. As Ra slightly exceeds 10^3, χ exhibits a pronounced increase, reaching values approximately 20% higher than χ_{uni}, before converging back to the homogeneous value at higher Rayleigh numbers. This behavior indicates that small-scale heterogeneity affects mass transfer efficiency only within a narrow transitional regime, Rayleigh-Darcy convection evolves from stable convective rolls to a chaotic flow state.

In contrast, for larger correlation lengths $\mathcal{L} > 0.1$, the scalar dissipation χ is significantly reduced relative to χ_{uni} across the entire range of Rayleigh numbers considered, indicating a persistent modulation of the convective flow patterns by strong heterogeneity. We further characterize the dependence of fluctuation energy on the correlation length $\mathcal{L}$ and the Rayleigh number Ra. Figure 3(b) shows the ratio E/E_{uni}, where E_{uni} denotes the fluctuation energy in the homogeneous medium. As the Rayleigh number approaches the critical value $Ra \approx 1300$, flow fluctuations become markedly stronger than in the homogeneous case, whereas they converge back to the homogeneous behavior when $Ra > 7500$. In Fig. 3(c), we plot the wall-normal profiles of the time-averaged concentration-gradient magnitude $\langle\overline{|\nabla c|^2}\rangle$ with different correlation lengths. As the Rayleigh number Ra increases, the dissipation becomes increasingly concentrated near the boundaries, revealing enhanced

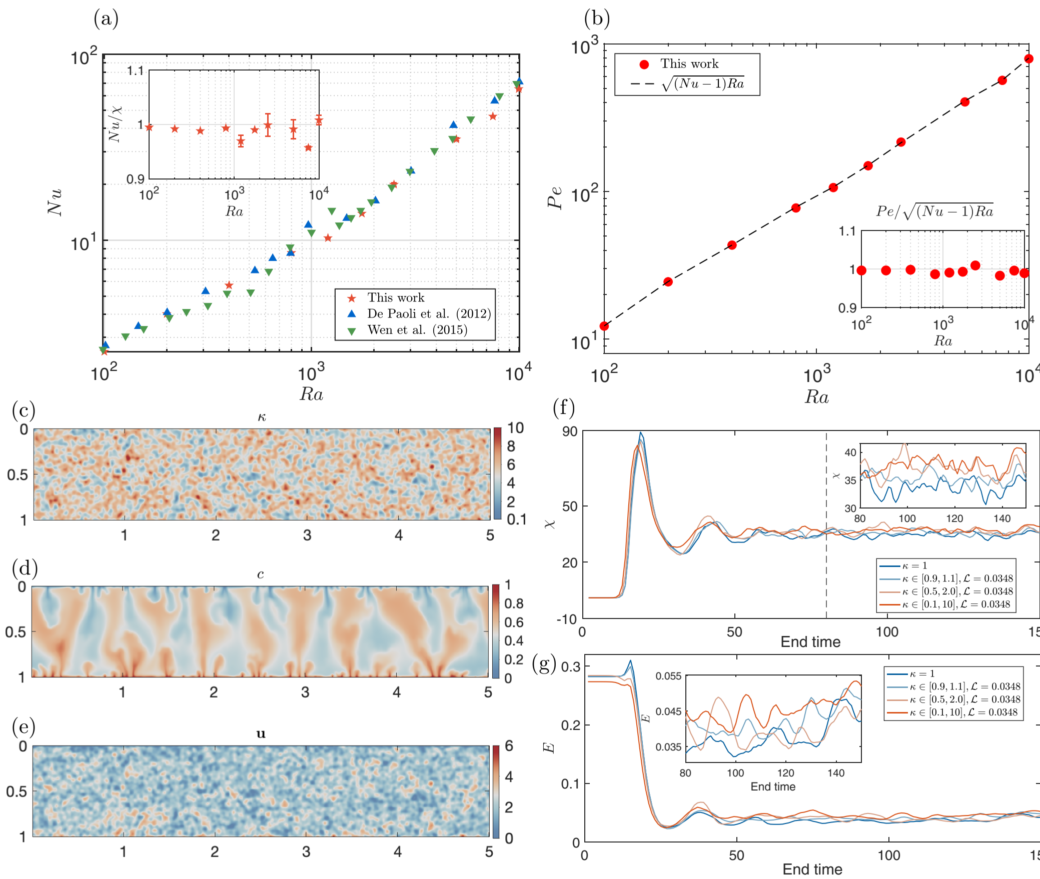

FIG. 2. (a) Nusselt number Nu as a function of Ra for the homogeneous case; the inset shows the scaling $\chi \approx Nu$. (b) Péclet number Pe as a function of Ra for the homogeneous case; the inset shows the scaling $Pe \approx \sqrt{(Nu-1)Ra}$. (c) Spatial distribution of the permeability field with $\kappa \in [0.1, 10]$ and correlation length $\mathcal{L} = 0.0348$. (d) Corresponding instantaneous concentration field c and (e) characteristic velocity magnitude $|\mathbf{u}|$ at $t^*/t_c = 100$ and $Ra = 5000$. (f) Temporal evolution of the scalar dissipation rate χ for $\mathcal{L} = 0.0348$ and $\kappa \in [0.1, 10]$ at $Ra = 5000$; the inset shows the late-time evolution over $t^*/t_c \in [80, 150]$. (g) Temporal evolution of the fluctuation energy E for the same case; the inset shows the late-time evolution over $t^*/t_c \in [80, 150]$.

near-wall scalar transport efficiency, consistent with previously reported results for homogeneous media [34,35].

The above observations highlight that (i) two critical Rayleigh numbers exist, with the first $\approx$1300 dividing the RDC pattern into two distinct regimes, and the second $\approx$7500 marking the disappearance of extra fluctuation energy; and (ii) heterogeneity with small correlation length ($\mathcal{L} \ll 1$) and with large correlation length ($\mathcal{L} > 0.1$) modulates convective patterns in fundamentally different ways. Understanding how heterogeneity reshapes RDC thus requires linking permeability-induced flow modifications to convection length scales across different regimes.

A. The low–Rayleigh-number regime

We first look into the low–Rayleigh-number regime, $Ra < 1300$. Figures 4(a)–4(c) show the permeability fields for a homogeneous medium and heterogeneous media with correlation lengths $\mathcal{L} = 0.0348$ and $\mathcal{L} = 0.464$, respectively, together with time-averaged streamlines at $Ra = 400$,

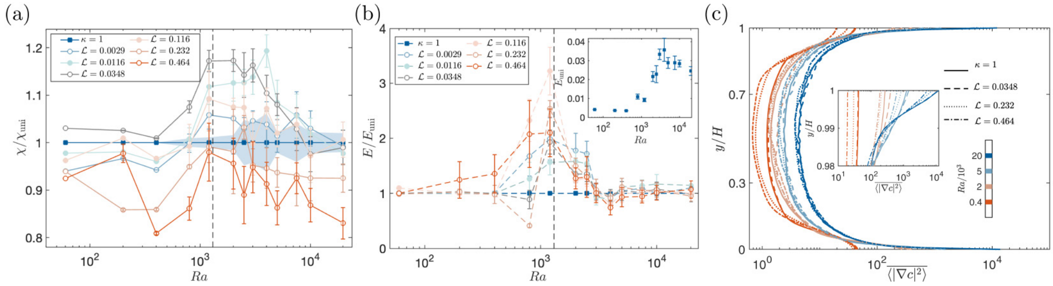

FIG. 3. (a) Variation of $\chi/\chi_{\rm uni}$ with Ra. The shaded band indicates the steady-state variability of the uniform case, the black dotted line marks $Ra = 1300$, and the vertical bars denote the standard deviation at each Ra. (b) Variation of $E/E_{\rm uni}$ with Ra. The black dotted line marks $Ra = 1300$, and the vertical bars denote the standard deviation at each Ra. Inset: $E_{\rm uni}$ for the uniform case. In the first two snapshots, different colors correspond to different correlation lengths $\mathcal{L}$. (c) Variation of $\overline{\langle|\nabla c|^2\rangle}$ with Ra for different $\mathcal{L}$. Inset: boundary-layer contribution to $\overline{\langle|\nabla c|^2\rangle}$ versus Ra ($y/H \in [0.98, 1]$). In the third snapshot, different line styles denote different correlation lengths $\mathcal{L}$, whereas different colors denote different Rayleigh numbers.

and the corresponding scalar concentration c and scalar dissipation $|\nabla c|^2$ fields. In this regime, the convection structures present representative rolls and remain essentially steady in time. For the homogeneous case and the weakly heterogeneous medium with $\mathcal{L} = 0.0348$, the overall roll morphology is nearly identical, with only mild small-scale distortions. These distortions slightly deform the plume shapes and change the effective contact area between adjacent plumes, but do not alter the global flow topology, as shown in Figs. 4(g) and 4(h). As a result, the enhancement of scalar transport is limited, and the mean scalar dissipation differs by less than 5% from that of the homogeneous case.

However, for a large permeability correlation length $\mathcal{L} = 0.464$ as shown in Figs. 4(f) and 4(i), the concentration field and the associated scalar dissipation are strongly controlled by the medium heterogeneity, leading to a pronounced reorganization of the convective pattern. The resulting convection rolls are fewer in number and exhibit reduced morphological symmetry, with the onset of convective instability closely correlated with the spatial distribution of permeability. This structural control suppresses spatially random plume formation and localizes strong scalar gradients primarily at the interfaces between high- and low-permeability regions. Consequently, high-permeability pathways are characterized by enhanced advection and more uniform concentration fields, whereas low-permeability regions exhibit reduced transport and weaker dissipation.

The statistical signature of this behavior is evident in the probability density functions of $|\nabla c|^2$ shown in Fig. 4(j). For the homogeneous case and small correlation lengths, the distributions exhibit a sharp primary peak, revealing relatively uniform local mixing. In contrast, for $\mathcal{L} = 0.464$ the distribution shifts toward lower gradient values, accompanied by a marked reduction of the primary peak and an increased probability weight at low gradients. This confirms that large permeability correlation lengths significantly suppress scalar dissipation by concentrating strong gradients at permeability interfaces. Notably, regions of extremely low scalar dissipation are predominantly located within high-permeability pathways, where fast and wide plumes result in a more homogeneous concentration field with weak gradients.

We characterize the dominant convective length scale using the interior contribution to the scalar dissipation, which scales as $\chi_{\rm bulk} \sim D(\Delta c)^2 H^{-2} Pe\,(\ell/H)$, where the cell width ℓ/H is defined as the wavelength associated with the mean wavenumber $\overline{k}$ obtained from an FFT analysis at midheight ($z/H = 0.5$) [34]. This is the cell width ℓ/H, which represents the characteristic spacing between neighboring convective plumes and controls scalar exchange in the bulk. As shown in Fig. 4(k), the plume spacing in the homogeneous case follows the scaling $\ell/H \sim \alpha_1 Ra^{-5/14}$, consistent with [9], with a fitted prefactor $\alpha_1 \approx 3.39$. This scaling remains valid throughout the cell-dominated

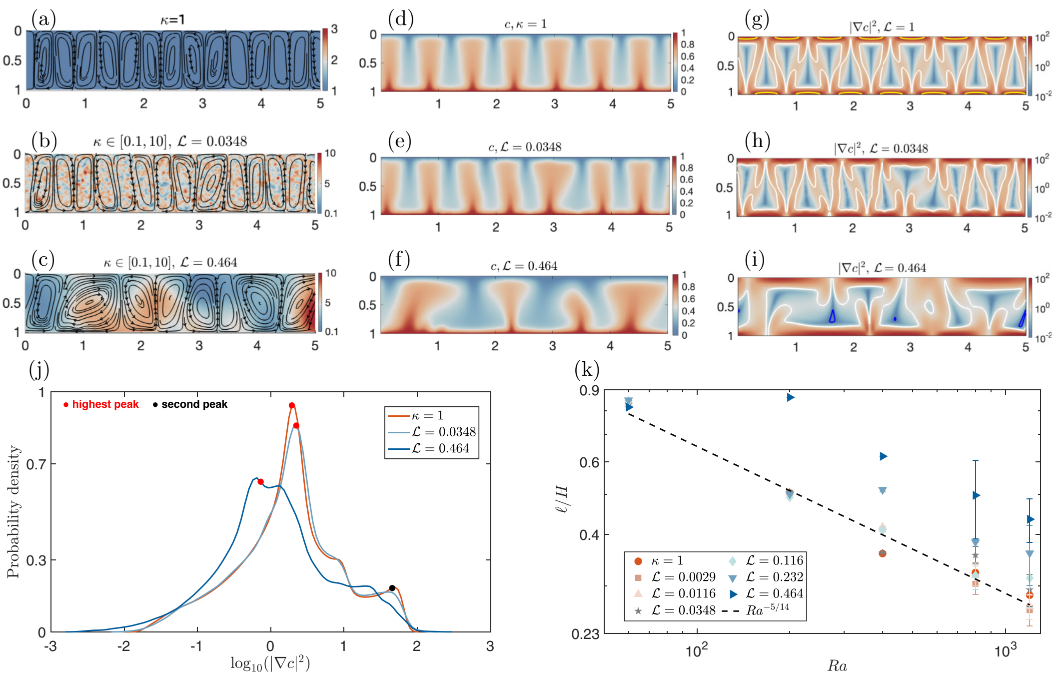

FIG. 4. Snapshots (a)–(c) show spatial distributions for the homogeneous case ($\kappa = 1$) and heterogeneous cases with different correlation lengths $\mathcal{L}$ at $Ra = 400$, together with the corresponding time-averaged streamlines. Snapshots (d)–(f) show instantaneous concentration fields at $t^*/t_c = 120$ with the corresponding permeability fields. Snapshots (g)–(i) show time-averaged scalar dissipation fields over $t^*/t_c \in [100, 120]$, where blue contours indicate regions of lower dissipation. Snapshot (j) shows probability density functions of $|\nabla c|^2$ for different $\mathcal{L}$; the highest-probability regions identified in (g)–(i) are marked by white contours and secondary peaks by yellow contours. Snapshot (k) shows the mean plume spacing ℓ/H as a function of Ra.

regime ($Ra < 1300$). When permeability heterogeneity is introduced, the characteristic length scale increases systematically with the correlation length. For $\mathcal{L} > 0.1$, ℓ/H exceeds the homogeneous prediction, reflecting the increasing control exerted by the heterogeneous permeability field.

B. The middle-Rayleigh-number regime

We then examine a higher Rayleigh number ($Ra = 2000$), which is slightly above the critical value. Figures 5(a)–5(c) show that at such a Rayleigh number the flow no longer maintains the ordered convective structures observed at lower Ra, but instead transitions to an unsteady, multiscale convective regime [19]. In this regime, numerous small-scale plumes continuously emerge from the boundary layers and generate localized motions. As they rise, these plumes progressively merge into energetic columnar mega-plumes that dominate the large-scale circulation in the bulk. As a result, both advection and the dominant contribution to scalar dissipation are largely confined to the near-boundary microplume layer. Permeability heterogeneity modifies the plume morphology relative to the homogeneous case for both small and large correlation lengths. For small correlation lengths, heterogeneity disturbs the merging of intermittent microplumes near the boundary and thereby enhances local instability, leading to the formation of numerous microplumes within the boundary layer, while the overall convective organization and dominant length scale remain largely unchanged. In contrast, for large correlation lengths, the convection undergoes a pronounced structural reorganization. The plumes become fewer in number, highly asymmetric, and spatially localized, indicating that the convective pattern is strongly controlled by the underlying permeability structure rather than by intrinsic convective instability.

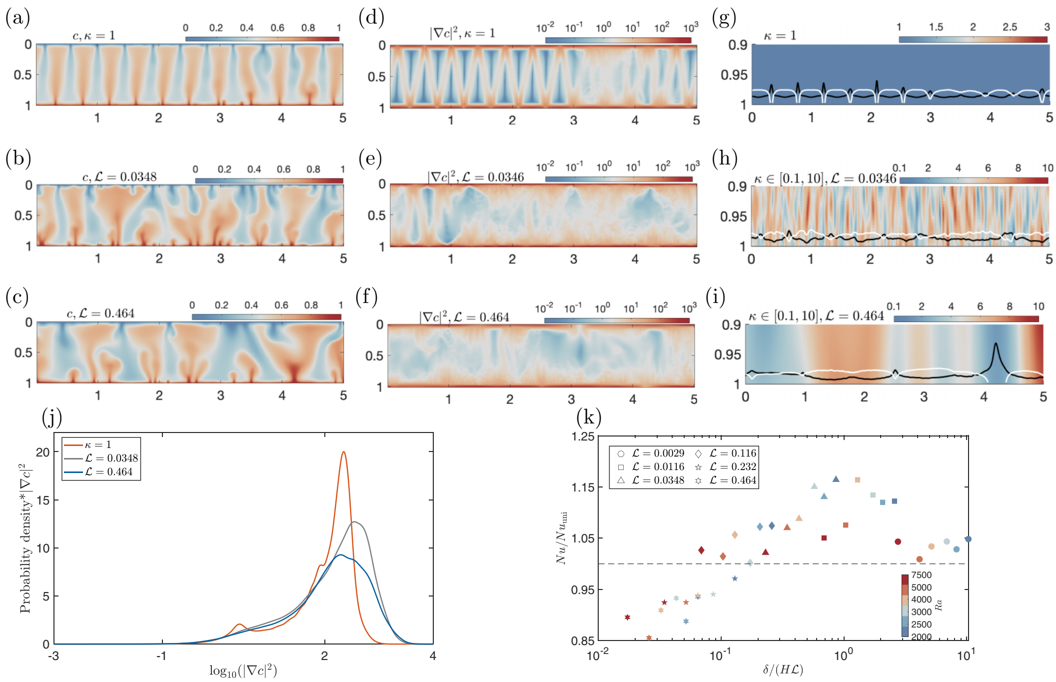

FIG. 5. Snapshots (a)–(c) show instantaneous concentration fields for the homogeneous case ($\kappa = 1$) and heterogeneous cases with different correlation lengths $\mathcal{L}$ at $Ra = 2000$ and $t^*/t_c = 200$. Snapshots (d)–(f) display the time-averaged scalar dissipation fields over the statistically steady interval $t^*/t_c \in [100, 200]$. Snapshots (g)–(i) present enlarged views of the upper boundary layer ($y/H \in [0.9, 1]$) for the homogeneous and heterogeneous cases with different correlation lengths $\mathcal{L}$, together with the concentration contour $c = 0.8$ (black line) and the scalar dissipation contour $\log_{10}(|\nabla c|^2) = 2$ (white line). Snapshot (j) shows the weighted probability distributions of $|\nabla c|^2$ for different $\mathcal{L}$, where the ordinate represents $|\nabla c|^2$ multiplied by its probability density. Snapshot (k) shows the relationship between $\delta/(H\mathcal{L})$, the ratio of the boundary-layer thickness to the correlation length, and the normalized transport efficiency Nu/Nu_{uni}.

The time-averaged scalar dissipation fields ($|\nabla c|^2$) for the homogeneous case and two stochastic permeability realizations with distinct correlation lengths ($\mathcal{L} = 0.0348$ and $\mathcal{L} = 0.464$) are compared in Figs. 5(d)–5(f). In the homogeneous case, scalar dissipation is primarily concentrated within the upper and lower boundary layers, forming continuous and nearly periodic high-dissipation bands. Introducing permeability heterogeneity substantially modifies this distribution. For small $\mathcal{L} = 0.0348$, numerous patchy regions of elevated dissipation emerge in the bulk, reflecting enhanced local unsteadiness induced by small-scale permeability fluctuations. In contrast, for large $\mathcal{L} = 0.464$, the boundary-layer dissipation becomes intermittent and strongly spatially nonuniform.

To further elucidate the correlation between the permeability field and boundary-layer morphology, we superimpose the permeability distribution within $y/H \in [0.9, 1]$ with the corresponding time-averaged concentration contours and time-averaged scalar-dissipation contours that delineate the boundary layer, as shown in Figs. 5(g)–5(i). For small correlation lengths, although numerous microplumes are observed instantaneously, the corresponding time-averaged concentration fields remain relatively smooth. This indicates that the enhanced boundary-layer instability primarily manifests through continuous microplume generation and merging, rather than through persistent large-scale reorganization. Consistently, the time-averaged scalar dissipation exhibits pronounced spatial variability, characterized by alternating regions of high and low dissipation—a feature that becomes particularly prominent for large correlation lengths. For large correlation lengths, the boundary-layer thickness becomes thinner in high-permeability regions and thicker in low-permeability regions, synchronizing with local permeability variations. Moreover, in low-permeability zones, the scalar dissipation exhibits distinct spatial discontinuities, reflecting a major suppression of local transport and pronounced modulation of convective activity by permeability heterogeneity.

Figure 5(j) shows the weighted probability distributions of $|\nabla c|^2$ for $Ra = 2000$. For $\mathcal{L} = 0.0348$, the distribution shifts toward larger values of $|\nabla c|^2$, producing a pronounced peak that reflects enhanced boundary-layer dissipation and a reduced contribution from the bulk region. As $\mathcal{L}$ increases to 0.464, the peak broadens and shifts toward lower $|\nabla c|^2$, indicating weakened boundary-layer intermittency. Recall that a peak exists in the normalized dissipation–Rayleigh-number curve, as shown in Fig. 3(a). This behavior can be further understood by examining the interplay between the boundary-layer thickness and the heterogeneity correlation length in Fig. 5(k). The boundary-layer thickness follows the scaling $\delta/H \sim \alpha_2/Ra$ with $\alpha_2 = 60$, consistent with the scaling assumption adopted throughout this manuscript. The influence of $(\delta/H)/\mathcal{L}$ on vertical transport efficiency is clearly nonmonotonic. When $(\delta/H)/\mathcal{L} \ll 1$, scalar dissipation is suppressed relative to the homogeneous case. As $(\delta/H)/\mathcal{L}$ approaches unity, the transport efficiency increases and can exceed that of the homogeneous case. With a further increase in $(\delta/H)/\mathcal{L}$, however, the effect of heterogeneity gradually weakens. This nonmonotonic behavior reflects the competition between the heterogeneity correlation length and the intrinsic flow-structure length scale: the smaller scale tends to dominate the transport pattern, whereas the strongest coupling arises when the two are of comparable magnitude.

C. The large-Rayleigh-number regime

We next consider the large-Rayleigh-number regime and investigate the cases with $Ra = 20\,000$. At this high Rayleigh number, the boundary layer thickness ($\sim 60/Ra$) is smaller than all $\mathcal{L}$ adopted in this study and is negligible compared to H. The mean scalar dissipation χ is reduced by approximately 20% for the largest correlation length ($\mathcal{L} = 0.464$), whereas for small correlation lengths $\chi/\chi_{\text{uni}} \approx 1$, indicating convergence toward the homogeneous limit. Instantaneous concentration fields at $t^*/t_c = 400$ for the homogeneous case and heterogeneous media with correlation lengths $\mathcal{L} = 0.0348$ and 0.464 are shown in Figs. 6(a)–6(c), revealing very similar convective patterns in the bulk region regardless of heterogeneity. We then focus on the near-boundary region ($y/H \in [0.975, 1]$) to compare the dissipation contours and concentration contours that delineate the boundary layer, as shown in Figs. 6(d)–6(f). The results show that small correlation lengths introduce very little variation in boundary-layer properties, whereas large correlation lengths substantially reshape the boundary-layer morphology. The dissipation spectra shown in Fig. 6(g) further support these observations. The dissipation spectra in the bulk region ($|\nabla c|^2 < 10^3$) for the three cases almost overlap, whereas those near the boundary ($|\nabla c|^2 > 10^3$) exhibit distinct shapes, with a much broader distribution and a lower peak emerging for the $\mathcal{L} = 0.464$ case.

We further compare the $c = 0.8$ isolines for different permeability correlation lengths [Fig. 6(h)]. An interesting finding is that the isoline for the $\mathcal{L} = 0.464$ case overlaps well with a reference profile constructed by rescaling the uniform boundary-layer thickness using the local permeability field along the boundary. This indicates that, at very high Rayleigh numbers where $\mathcal{L}$ is orders of magnitude larger than the characteristic flow-structure length scale, the boundary layer is predominantly local and can be described as a linear superposition of local permeability effects. Consequently, whether heterogeneity enhances or suppresses the global transport efficiency at such high Rayleigh numbers is determined by the permeability distribution along the boundary, which may vary substantially among different realizations of the random permeability field.

D. Coupled effects of porosity and permeability

In this subsection, we examine the coupled effects of heterogeneous porosity and permeability on scalar dissipation. The analysis focuses on the permeability range $\kappa \in [0.1, 10]$ and several

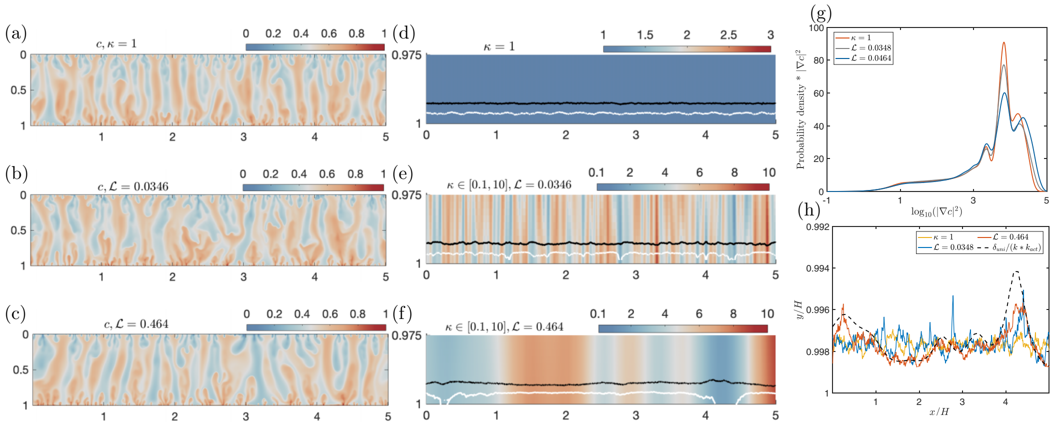

FIG. 6. Snapshots (a)–(c) show instantaneous concentration fields at $t^*/t_c = 400$ for the homogeneous medium ($\kappa = 1$) and heterogeneous media with $\kappa \in [0.1, 10]$ at correlation lengths $\mathcal{L} = 0.0348$ and 0.464, respectively, at $Ra = 20\,000$. Snapshots (d)–(f) show the permeability distribution within the near-boundary region ($y/H \in [0.975, 1]$), together with the contours $\log_{10}(|\nabla c|^2) = 3.7$ (white lines) and $\log_{10}(|\nabla c|^2) = 3$ (black lines). (g) Weighted probability distributions of $|\nabla c|^2$ for different correlation lengths $\mathcal{L}$, where the ordinate represents $|\nabla c|^2$ multiplied by its probability density. (h) Superposition of the $C = 0.8$ isolines for different permeability correlation lengths $\mathcal{L}$. The black dashed line obtained by scaling the uniform boundary-layer thickness with the normalized boundary permeability field corresponding to $\mathcal{L} = 0.464$.

representative correlation lengths $\mathcal{L}$. Accordingly, the dimensionless governing equations in (4) are modified to account for porosity variations as

$$\frac{\partial c}{\partial t} + \nabla \cdot \left(\frac{c\mathbf{u}}{\phi} - \frac{1}{\mathrm{Ra}} \nabla c \right) = 0, \quad \nabla \cdot \mathbf{u} = 0, \quad \mathbf{u} = -\kappa_{\mathrm{act}} (\nabla p + c\,\mathbf{i}), \tag{4}$$

where the permeability κ_{act} and porosity ϕ are assumed to be related [36] through

$$\kappa_{\mathrm{act}} = \kappa_{0,\mathrm{act}} * (\phi/\phi_0)^3,$$

where $\kappa_{0,\mathrm{act}}$ and ϕ_0 are fixed at 1. The porosity fields corresponding to two different correlation lengths are presented in Figs. 7(a) and 7(b), and all other parameter settings remain the same as those in the previous subsection.

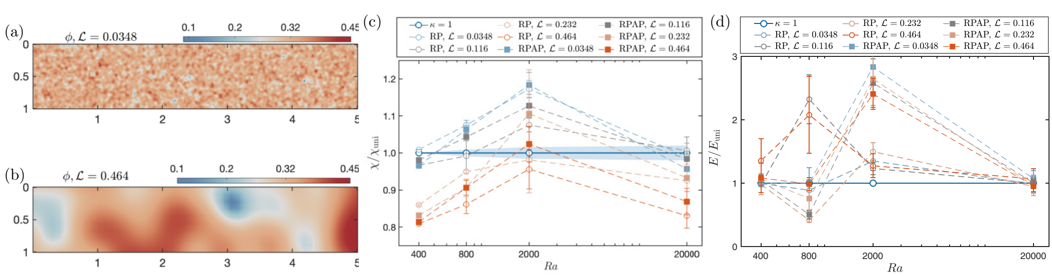

FIG. 7. (a) Porosity field with correlation length $\mathcal{L} = 0.0348$. (b) Porosity field with correlation length $\mathcal{L} = 0.464$. (c) χ/χ_{uni} versus Ra. The shaded band indicates the variability of the uniform case, and the vertical bars denote the standard deviation. (d) E/E_{uni} versus Ra. The shaded band indicates the variability of the uniform case, and the vertical bars denote the standard deviation. In both figures, RP denotes random permeability, whereas RPAP denotes combined random permeability and porosity.

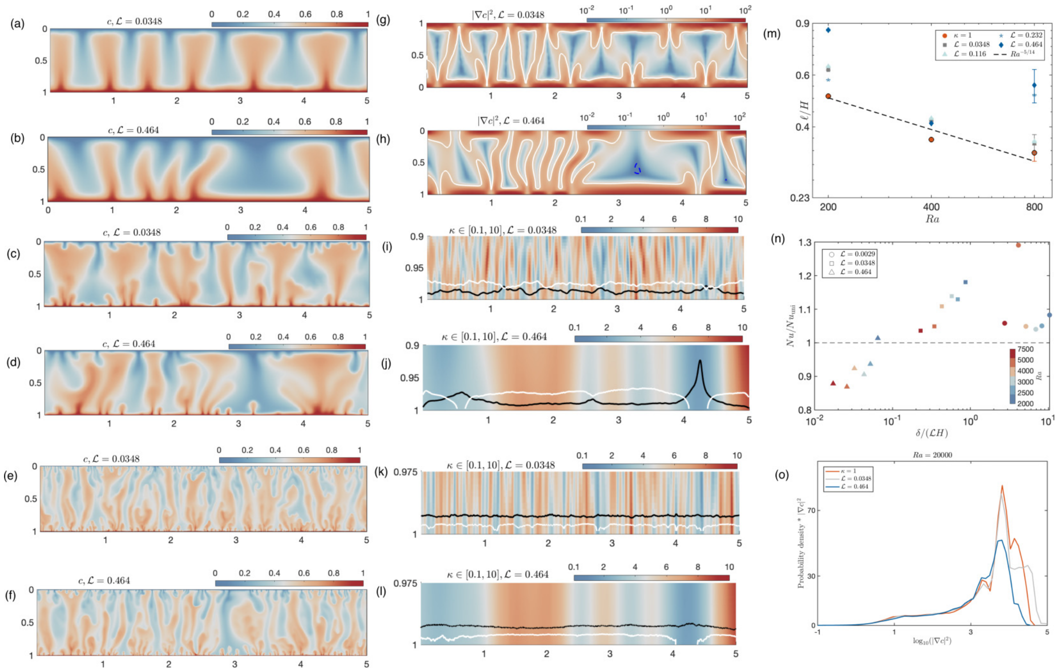

FIG. 8. (a)–(f) Instantaneous concentration fields at $t^*/t_c = 120, 200, 400$ for heterogeneous porosity-permeability cases with $\kappa \in [0.1, 10]$ and correlation lengths $\mathcal{L} = 0.0348$ and 0.464, at $Ra = 400, 2000, 20\,000$, respectively. (g) and (h) Corresponding time-averaged scalar-dissipation fields over $t^*/t_c \in [100, 120]$ at $Ra = 400$. The blue contour denotes the lower-dissipation region, and the white contour denotes the highest peak of probability density functions of $|\nabla c|^2$. (i) and (j) Permeability fields for the two correlation lengths, together with enlarged views of the upper boundary layer ($y/H \in [0.9, 1]$) for the heterogeneous porosity-permeability cases. The concentration contour $c = 0.8$ is shown in black, and the scalar-dissipation contour $\log_{10}(|\nabla c|^2) = 2$ is shown in white. (k) and (l) Enlarged views of the upper boundary layer ($y/H \in [0.975, 1]$) for the heterogeneous porosity-permeability cases with different correlation lengths. The contour $\log_{10}(|\nabla c|^2) = 3$ is shown in black, and the contour $\log_{10}(|\nabla c|^2) = 3.7$ is shown in white. (m) Mean plume spacing ℓ/H as a function of Ra. (n) Relationship between $\delta/(H\mathcal{L})$, the ratio of the boundary-layer thickness to the correlation length, and the normalized transport efficiency Nu/Nu_{uni}. (p) Weighted probability distributions of $|\nabla c|^2$ for different $\mathcal{L}$, where the ordinate denotes $|\nabla c|^2$ multiplied by its probability density at $Ra = 20\,000$.

Figures 8(a)–8(f) show the instantaneous concentration fields for $Ra = 400$, 2000, and 20 000 at $t/t_c = 120$, 200, and 400, respectively. In most cases, the concentration fields remain broadly similar to those in the uniform-porosity case, suggesting that porosity heterogeneity has only a limited influence on the large-scale flow structure. A noticeable difference appears only for $Ra = 400$ at the large correlation length $\mathcal{L} = 0.464$. Figures 8(g) and 8(h) provide enlarged views of the scalar-dissipation fields at $Ra = 400$ for two representative correlation lengths, $\mathcal{L} = 0.0348$ and $\mathcal{L} = 0.464$. Compared with the permeability-only heterogeneous case, the coupled porosity-permeability heterogeneous case shows a smaller low-dissipation region, indicating that scalar transport becomes more concentrated in the high-permeability regions, while it is further suppressed in the low-permeability regions. Consistently, the near-wall enlarged views in Figs. 8(i)–8(l), with concentration and scalar-dissipation contours overlaid at different values of y/H, show that the difference between the constant-porosity and heterogeneous-porosity cases generally decreases as Ra increases.

For the heterogeneous porosity-permeability cases, Figs. 8(m)–8(o) presents the plume spacing, the interplay between the boundary-layer thickness and the heterogeneity correlation length, and the

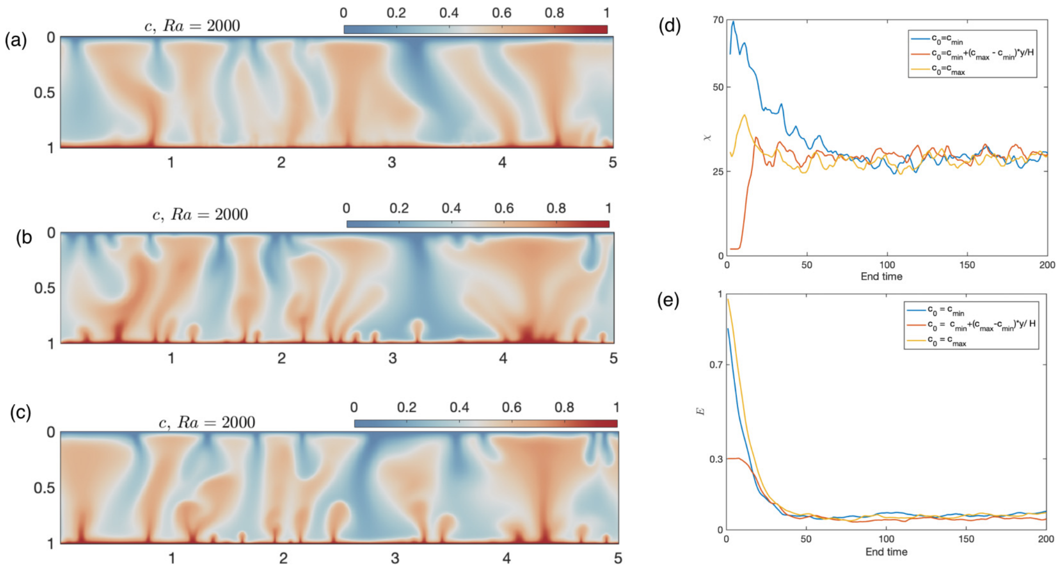

FIG. 9. Snapshots (a)–(c) show the concentration fields at $t/t_c = 200$ corresponding to the three initial conditions: $c_0 = 0$, $c_0 = y/H$, and $c_0 = 1$, respectively. In each case, a small perturbation is superimposed on the initial concentration field. Snapshot (d) shows the time evolution of the scalar dissipation rate χ, and snapshot (e) shows the time evolution of the fluctuation energy E. All other parameters are the same as those used in the previous simulations.

probability density of $\log_{10}(|\nabla c|^2)$ weighted by $|\nabla c|^2$, respectively. Compared with the uniform-porosity case, the introduction of porosity heterogeneity does not lead to significant changes in the overall transport behavior, although it slightly modulates the flow structure and scalar-dissipation distribution in different flow regimes. For low Ra ($Ra < 1300$), convection remains steady and roll-like, and porosity heterogeneity mainly increases the spatial irregularity of the concentration and scalar-dissipation fields without fundamentally altering the overall transport regime. At intermediate Ra ($1300 \lesssim Ra \lesssim 7500$), although the overall concentration pattern remains broadly similar, plume penetration and boundary-layer thickness are moderately modulated by the local medium properties. This modulation enhances spatial intermittency and makes mass transfer slightly more uneven. For high Ra ($Ra > 7500$), however, the influence of random porosity becomes much weaker, and both the large-scale flow structures and the scalar-dissipation statistics remain close to those obtained without porosity heterogeneity.

Overall, these results indicate that the transport efficiency in the porosity-permeability heterogeneous cases largely inherits the behavior of the permeability-only heterogeneous case.

E. The effects of initial condition

In this section, we examine the effects of the initial concentration distribution on the mass-transfer efficiency and the fluctuation energy. Based on (4), we consider the case with $\kappa \in [0.1, 10]$, $\mathcal{L} = 0.464$, and $Ra = 2000$. Three initial concentration distributions are tested: a uniform low-concentration state, $c_0 = 0$; a vertically linear profile, $c_0 = y/H$; and a uniform high-concentration state, $c_0 = 1$. In all cases, a small perturbation is added to trigger the instability, while all other parameters are kept the same as in the previous simulations. Figure 9 shows that the initial concentration distribution mainly affects the early transient evolution, whereas its influence on the long-time state is weak. As shown in Figs. 9(a)–9(c), all three cases eventually develop similar large-scale convective structures, despite some differences in local plume morphology. Figure 9(d) shows that the scalar dissipation rate χ depends strongly on the initial condition at early times, but the three curves gradually converge to a similar statistically steady level. A similar behavior is observed in Fig. 9(e) for the fluctuation energy E, although the initial values and decay rates differ, all cases eventually collapse to a narrow range with only small residual fluctuations. These results indicate that the initial concentration field mainly modifies the transient adjustment process, but does not significantly affect the final quasisteady convective state. Therefore, the analyses in the previous sections focus on the statistically steady regime, where the influence of the initial concentration distribution is negligible.

IV. CONCLUSION

Rayleigh-Darcy convection in heterogeneous porous media is investigated to elucidate how heterogeneity regulates convective patterns and controls vertical scalar transport efficiency. The results show that the interplay between intrinsic convective length scales and the heterogeneity correlation length $\mathcal{L}$ strongly influences RDC dynamics and transport, with distinct mechanisms operating across flow regimes.

For $Ra < 1300$, the flow is dominated by large-scale convection rolls spanning the full layer height, and transport is controlled primarily by the characteristic roll width ℓ/H. In this regime, only heterogeneity with a correlation length $\mathcal{L}$ comparable to ℓ/H can effectively distort roll morphology and regulate vertical transport.

For $1300 < Ra < 7500$, transport is no longer governed by coherent, domain-scale rolls but instead becomes dominated by small-scale circulations developing near the boundaries, associated with interactions among protoplumes. In this regime, the permeability correlation length becomes comparable to the boundary-layer thickness, so that heterogeneity perturbs the near-wall region, promotes the formation of numerous microplumes, and enhances local mixing.

For $Ra > 7500$, the boundary layer becomes thinner, and numerous microplumes are apparent near the boundaries. Heterogeneity therefore exerts a significant influence only when $\mathcal{L}$ is sufficiently large, by locally reshaping the boundary-layer thickness through permeability variations.

We further show that the considering porosity-permeability correlation and different initial scalar field do not qualitatively change the conclusions. This study provides fundamental insights into buoyancy-driven convection in realistic geological formations. Future work should extend the present framework to incorporate multiple driving mechanisms (e.g., coupled concentration and temperature gradients), and more complex boundary conditions, to capture the inherently multiscale transport processes in geological systems.

ACKNOWLEDGMENTS

The authors would like to thank Dr. Marco De Paoli for inspiring discussion in InterPore2025 and Dr. Yantao Yang for useful advice. This work was partially supported by the National Key Research and Development Program of China under Grant No. 2021YFA0717200, the National Natural Science Foundation of China under Grant No. 12371366, and the China Postdoctoral Science Foundation under Grants No. BX20240003 and No. 2025M773051. We gratefully thanks the support by the China National Petroleum Corporation–Peking University Strategic Cooperation Project for Fundamental Research.

DATA AVAILABILITY

The data that support the findings of this article are openly available [37].

[1] D. A. Nield and A. Bejan, *Convection in Porous Media* (Springer, New York, NY, 2006).

[2] A. G. Hunt and M. Sahimi, Flow, transport, and reaction in porous media: Percolation scaling, critical-path analysis, and effective medium approximation, Rev. Geophys. **55**, 993 (2017).

[3] H. Erfani, M. Babaei, and V. Niasar, Dynamics of CO_2 density-driven flow in carbonate aquifers: Effects of dispersion and geochemistry, Water Resour. Res. **57**, e2020WR027829 (2021).
[4] M. De Paoli, F. Zonta, and A. Soldati, Influence of anisotropic permeability on convection in porous media: Implications for geological CO_2 sequestration, Phys. Fluids **28**, 056601 (2016).
[5] H. E. Huppert and J. A. Neufeld, The fluid mechanics of carbon dioxide sequestration, Annu. Rev. Fluid Mech. **46**, 255 (2014).
[6] I. J. Winograd, Radioactive waste disposal in thick unsaturated zones, Science **212**, 1457 (1981).
[7] A. Jin and S.-Y. Chang, Radioactive contaminant transport in subsurface porous environment, in *Proceedings of the 2007 National Conference on Environmental Science and Technology*, edited by E. Nzewi, G. Reddy, S. Luster-Teasley, V. Kabadi, S.-Y. Chang, K. Schimmel, and G. Uzochukwu (Springer, New York, NY, 2009), pp. 181–188.
[8] P. Cheng, Heat transfer in geothermal systems, Adv. Heat Transf. **14**, 1 (1978).
[9] D. R. Hewitt, J. A. Neufeld, and J. R. Liste, Stability of columnar convection in a poromedium, J. Fluid Mech. **737**, 205 (2013).
[10] P. Talebizadeh Sardari, G. S. Walker, M. Gillott, D. Grant, and D. Giddings, Numerical modelling of phase change material melting process embedded in porous media: Effect of heat storage size, Proc. Inst. Mech. Eng., Part A: J. Power Energy **234**, 365 (2020).
[11] H. Zheng, C. Wang, Q. Liu, Z. Tian, and X. Fan, Thermal performance of copper foam/paraffin composite phase change material, Energy Convers. Manage. **157**, 372 (2018).
[12] D. R. Hewitt, Vigorous convection in porous media, Proc. R. Soc. A **476**, 20200111 (2020).
[13] M. De Paoli, Convective mixing in porous media: A review of Darcy, pore-scale and Hele-Shaw studies, Eur. Phys. J. E **46**, 129 (2023).
[14] S. Pirozzoli, M. De Paoli, F. Zonta, and A. Soldati, Towards the ultimate regime in Rayleigh–Darcy convection, J. Fluid Mech. **911**, R4 (2021).
[15] J. J. Hidalgo, J. Fe, L. Cueto-Felgueroso, and R. Juanes, Scaling of convective mixing in porous media, Phys. Rev. Lett. **109**, 264503 (2012).
[16] M. De Paoli, G. S. Yerragolam, D. Lohse, and R. Verzicco, AFiD-Darcy: A finite difference solver for numerical simulations of convective porous media flows, Comput. Phys. Commun. **282**, 108524 (2023).
[17] D. R. Hewitt, J. A. Neufeld, and J. R. Lister, Ultimate regime of high Rayleigh number convection in a porous medium, Phys. Rev. Lett. **108**, 224503 (2012).
[18] B. Wen, L. T. Corson, and G. P. Chini, Structure and stability of steady porous medium convection at large Rayleigh number, J. Fluid Mech. **772**, 197 (2015).
[19] J. Otero, L. A. Dontcheva, H. Johnston, R. A. Worthing, A. Kurganov, G. Petrova, and C. R. Doering, High-Rayleigh-number convection in a fluid-saturated porous layer, J. Fluid Mech. **500**, 263 (2004).
[20] J. J. Hidalgo, M. Dentz, Y. Cabeza, and J. Carrera, Dissolution patterns and mixing dynamics in unstable reactive flow, Geophys. Res. Lett. **42**, 6357 (2015).
[21] C. Hu, K. Xu, and Y. Yang, Effects of the geothermal gradient on the convective dissolution in CO_2 sequestration, J. Fluid Mech. **963**, A23 (2023).
[22] A. C. Slim, Solutal-convection regimes in a two-dimensional porous medium, J. Fluid Mech. **741**, 461 (2014).
[23] Y. Liang, B. Wen, M. A. Hesse, and D. DiCarlo, Effect of dispersion on solutal convection in porous media, Geophys. Res. Lett. **45**, 9690 (2018).
[24] D. Daniel and A. Riaz, Effect of viscosity contrast on gravitationally unstable diffusive layers in porous media, Phys. Fluids **26**, 116601 (2014).
[25] R. Benhammadi and J. J. Hidalgo, Impact of porous media heterogeneity on convective mixing in a Rayleigh-Bénard instability, Adv. Water Resour. **206**, 105139 (2025).
[26] R. Benhammadi, P. Meunier, and J. J. Hidalgo, Experimental and numerical study of CO_2 dissolution in a heterogeneous Hele-Shaw cell, Phys. Rev. Fluids **10**, 043501 (2025).
[27] R. Benhammadi, A. De Wit, and J. J. Hidalgo, Effect of permeability heterogeneity on reactive convective dissolution, Phys. Rev. Fluids **10**, 123501 (2025).
[28] R. Nussbaumer, G. Mariethoz, E. Gloaguen, and K. Holliger, Which path to choose in sequential Gaussian simulation, Math. Geosci. **50**, 97 (2018).

[29] R. Nussbaumer, G. Mariethoz, M. Gravey, E. Gloaguen, and K. Holliger, Accelerating sequential Gaussian simulation with a constant path, Comput. Geosci. **112**, 121 (2018).
[30] T. Cheng, H. Yang, and S. Sun, Parallel fully coupled methods for bound-preserving solution of subsurface flow and transport in porous media, J. Comput. Phys. **470**, 111537 (2022).
[31] T. Cheng, H. Yang, C. Yang, and S. Sun, Scalable semismooth Newton methods with multilevel domain decomposition for subsurface flow and reactive transport in porous media, J. Comput. Phys. **467**, 111440 (2022).
[32] J. Tu, H. Yang, X. Chen, S. Sun, and T. Cheng, A scalable parallel reservoir simulator on corner-point grids for discontinuous Galerkin modeling of real-field geological reservoirs, J. Comput. Phys. **547**, 114546 (2026).
[33] S. Balay *et al.*, PETSc/TAO users manual, Technical Report ANL-21/39 (Argonne National Laboratory, Argonne, IL, 2023).
[34] X. Zhu, Y. Fu, and M. De Paoli, Transport scaling in porous media convection, J. Fluid Mech. **991**, A4 (2024).
[35] M. De Paoli, S. Pirozzoli, F. Zonta, and A. Soldati, Strong Rayleigh–Darcy convection regime in three-dimensional porous media, J. Fluid Mech. **943**, A51 (2022).
[36] M. Wapperom, X. Lyu, and D. Voskov, Accurate modeling of near-wellbore effects induced by supercritical CO2 injection, *ECMOR 2022* (European Association of Geoscientists & Engineers, 2022), Vol. 2022, pp. 1–13.
[37] T. Cheng, H. Yang, M. Zhang, and K. Xu, Simulation data for Rayleigh–Darcy convection in heterogeneous porous strata [data set] (Zenodo, Geneva, Switzerland, 2026), doi: 10.5281/zenodo.18449272.